AGU PUBLICATIONS

JGR

Journal of Geophysical Research: Atmospheres

RESEARCH ARTICLE
10.1002/2016JD024917

Key Points:
- ECMWF PWV shows a better performance than NCEP one as evaluated by radiosonde, GPS, and microwave satellite
- Upward global PWV trends are observed from five types of data sets in the period of 1979–2014 and become more apparent in recent years
- Positive PWV-temperature regression slopes are observed over most oceans, and negative values are found over many continents

Correspondence to:
Z. Liu,
lszzliu@polyu.edu.hk

Citation:
Chen, B., and Z. Liu (2016), Global water vapor variability and trend from the latest 36 year (1979 to 2014) data of ECMWF and NCEP reanalyses, radiosonde, GPS, and microwave satellite, *J. Geophys. Res. Atmos.*, *121*, 11,442–11,462, doi:10.1002/2016JD024917.

Received 6 FEB 2016
Accepted 21 SEP 2016
Accepted article online 25 SEP 2016
Published online 8 OCT 2016

Global water vapor variability and trend from the latest 36 year (1979 to 2014) data of ECMWF and NCEP reanalyses, radiosonde, GPS, and microwave satellite

Biyan Chen[1] and Zhizhao Liu[1]

[1]Department of Land Surveying and Geo-Informatics, Hong Kong Polytechnic University (PolyU), Kowloon, Hong Kong

Abstract The variability and trend in global precipitable water vapor (PWV) from 1979 to 2014 are analyzed using the PWV data sets from the ERA-Interim reanalysis of the European Centre for Medium-Range Weather Forecasts (ECMWF), reanalysis of the National Centers for Environmental Prediction (NCEP), radiosonde, Global Positioning System (GPS), and microwave satellite observations. PWV data from the ECMWF and NCEP have been evaluated by radiosonde, GPS, and microwave satellite observations, showing that ECMWF has higher accuracy than NCEP. Over the oceans, ECMWF has a much better agreement with the microwave satellite than NCEP. An upward trend in the global PWV is evident in all the five PWV data sets over three study periods: 1979–2014, 1992–2014, and 2000–2014. Positive global PWV trends, defined as percentage normalized by annual average, of $0.61 \pm 0.33\%$ decade^{-1}, $0.57 \pm 0.28\%$ decade^{-1}, and $0.17 \pm 0.35\%$ decade^{-1}, have been derived from the NCEP, radiosonde, and ECMWF, respectively, for the period 1979–2014. It is found that ECMWF overestimates the PWV over the ocean prior to 1992. Thus, two more periods, 1992–2014 and 2000–2014, are studied. Increasing PWV trends are observed from all the five data sets in the two periods: 1992–2014 and 2000–2014. The linear relationship between PWV and surface temperature is positive over most oceans and the polar region. Steep positive/negative regression slopes are generally found in regions where large regional moisture flux divergence/convergence occurs.

1. Introduction

As one of the water phases, water vapor carries a large amount of latent heat that can be released to the atmosphere via condensation and stored again through water evaporation [*Mohanakumar*, 2008; *Zhang et al*., 2013]. The variation of atmospheric precipitable water vapor (PWV) has a profound influence on global energy balance and climate system. Water vapor is also the most crucial greenhouse gas that accounts for about 60% of the natural greenhouse effect [*Wagner et al*., 2006; *Ahrens and Samson*, 2011].

Over the past four decades, the anthropogenic greenhouse gas emissions have significantly increased mainly due to the increased emission of carbon dioxide from fossil fuel combustion and industrial processes [*Intergovernmental Panel on Climate Change* (*IPCC*), 2015]. The increased greenhouse gases reduce the outgoing longwave radiation and contribute to the global warming phenomenon. Studies have shown that the global mean surface temperature has increased by 0.7–0.8°C since the beginning of the twentieth century [*Hansen et al*., 2001; *Smith and Reynolds*, 2005; *Parker et al*., 2007]. Atmospheric water vapor provides the single largest positive feedback on global warming [*Dai*, 2006; *Mieruch et al*., 2008; *Zhang et al*., 2013]. Both climate models and observations suggest that an upward trend in water vapor is expected to appear as a response to the surface temperature increase [*Held and Soden*, 2006; *Santer et al*., 2006; *Zhang et al*., 2013]. Monitoring the variation of atmospheric water vapor is thus significant not only for the detection of climate change but also for a better understanding of water vapor feedback on global warming.

Over the years, various investigations have been carried out with an effort to quantify the changes in the atmospheric water vapor. Water vapor data generally can be classified into two categories. The first category is observations from various sensors such as radiosonde [*Ross and Elliott*, 1996, 2001; *Zhai and Eskridge*, 1997; *Zhao et al*., 2012], Global Positioning System (GPS) [*Bock et al*., 2007; *Nilsson and Elgered*, 2008; *Vey et al*., 2010], satellite remote sensing [*Mieruch et al*., 2008, 2014; *Lu et al*., 2015], and weather stations [*Dai*, 2006]. The advantage of this category of data is that water vapor is directly measured at each station. However, it is difficult to derive an accurate PWV variation trend from the observational data since the observations are often incomplete and inhomogeneous and are sparsely distributed [*Dee et al*., 2011].

For example, operational radiosonde observations have merely about 900 globally distributed stations and they are available on the land only [*Niell et al*., 2001; *Kuo et al*., 2005]. Radiosonde observations provide the longest archival atmospheric water vapor and thus are often used in long-term climate research [*Liu et al*., 2015]. However, due to various reasons such as station removal, changes in instrument, or operating procedure, inhomogeneity often occurs causing artificial shifts in the radiosonde time series [*Easterling and Peterson*, 1995]. Therefore, long-term trends estimated from radiosonde observations may vary significantly due to different station selection criteria, quality control procedures, and bias corrections [*Dee et al*., 2011]. Another category of water vapor data is the reanalysis data set that is produced by assimilating various types of observations into a dynamically coherent data set based on an atmospheric general circulation model [*Trenberth and Smith*, 2005; *Wagner et al*., 2006; *Adler et al*., 2008; *Dessler and Davis*, 2010; *Zhang et al*., 2013]. Reanalysis data have advantages of global coverage, multivariable outputs, spatial integrity, and homogeneous record; thus, they can be of great value for atmospheric research such as climate change [*Allan*, 2002; *Dee et al*., 2011; *Lu et al*., 2015]. It should also be noted that reanalysis data may not be so reliable for areas where no or limited observations are available for the data assimilation [*Oikonomou and O'Neill*, 2006; *Sherwood et al*., 2010]. In addition, biases and errors in in situ and satellite observations that are assimilated into a reanalysis system may also degrade the system's performance. Thus, it is possible that products such as PWV trends derived from the reanalysis data may show spurious phenomenon.

Many studies have been reported concerning the atmospheric water vapor changes in different regions and different time periods. *Ross and Elliott* [2001] exploited the radiosonde observations to estimate the water vapor trends over the Northern Hemisphere in the period 1973–1995. That study showed that upward trends were seen at most stations of the Northern Hemisphere. *Bengtsson* [2004] calculated the global trends in PWV from the ERA-40 reanalysis of the European Centre for Medium-Range Weather Forecasts (ECMWF). For the period 1979–2001, the global PWV was found to have increased at a rate of 0.36 mm decade^{-1}. By using global meteorological data measured over 15,000 weather stations and marine ships, *Dai* [2006] derived the trends in global surface relative humidity (RH) during 1976–2004. Their study showed that large positive RH trends (0.5–2% decade^{-1}) occurred over the central and eastern United States, India, and western China, but RH decreased over eastern Australia and eastern Brazil. *Wagner et al*. [2006] reported a study on the global trends of water vapor observed by Global Ozone Monitoring Experiment (GOME). After excluding the El Niño–Southern Oscillation (ENSO) period 1997–1998, they found that the global water vapor increased by 2.8% ± 0.8% during the period 1996–2002. *Mieruch et al*. [2008] analyzed the global water vapor trends for an 11 year period (1996–2006) using satellite measurements derived from GOME and Scanning Imaging Absorption Spectrometer for Atmospheric Chartography (SCIAMACHY). Results showed that significant uptrends in water vapor were observed in Greenland, East Europe, Siberia, and Oceania; in addition, downtrends were seen in the northwest USA, Central America, Amazonia, Central Africa, and the Arabian Peninsula.

To extend our understanding of the climate system and how it responds to increasing greenhouse gas concentration, it is necessary to analyze the global water vapor distribution and changes in recent decades [*Schröder et al*., 2013]. Here we present a comprehensive analysis of the global PWV trends by examining five types of water vapor data sources: three from observations and two from models. This allows a careful intercomparison of results obtained from multiple data sources and an evaluation of the water vapor results from each source alone. In this paper, we adopt the latest ERA-Interim reanalysis of ECMWF to analyze the global water vapor variability and the trend for three periods: 1979–2014, 1992–2014, and 2000–2014. In addition, reanalysis products from the National Centers for Environmental Prediction (NCEP) are exploited to derive PWV trends for a direct comparison with ECMWF. Some previous studies indicated that reanalysis data are susceptible to time-varying biases; and therefore, the derived trends may not be reliable [*Bengtsson*, 2004; *Sherwood et al*., 2010]. Thus, water vapor data measured from radiosonde, GPS, and microwave satellite are also used to verify the reanalysis results. This paper is structured as follows. Descriptions of data sets from ECMWF, NCEP, radiosonde, GPS, and microwave satellite are given in section 2. In section 3, a study is carried out to evaluate the performance of ECMWF and NCEP by using PWV data from radiosonde, GPS, and microwave satellite. Section 4 presents the analysis of variability and trend in global water vapor from the five data sets. Finally, a summary of this study is given in section 5.

2. Data Description and Method

2.1. ERA-Interim Reanalysis

ERA-Interim is the latest global atmospheric reanalysis product produced by the ECMWF. It covers the period from 1 January 1979 onward and continuously extends forward in near real time [*Dee et al*., 2011]. The development of ERA-Interim is mainly to address some difficult data assimilation problems encountered during the production of ERA-40 [*Uppala et al*., 2005] as well as to improve the quality of the reanalysis products [*Dee et al*., 2011]. In the data assimilation, meteorological observations from various platforms, e.g., surface weather stations, ships, ocean buoys, radiosonde stations, aircraft, and remote sensing satellites, were assimilated into an atmospheric general circulation model to recreate the past atmospheric conditions [*Dee et al*., 2011].

In this paper, the global PWV data derived from the ECMWF ERA-Interim reanalysis for the period 1979–2014 are used. The spatial resolution of the ERA-Interim reanalysis PWV products used in this study is $1° \times 1°$ in latitude and longitude. The temporal resolution of the ECMWF-derived PWV data is 6 h. The monthly PWV data are obtained by averaging daily PWV data, and then the annual PWV data set is generated by averaging the monthly PWV data. In addition, the seasonal means are calculated for December-January-February (DJF), March-April-May (MAM), June-July-August (JJA), and September-October-November (SON) by averaging the monthly means in each season.

2.2. NCEP Reanalysis

The NCEP/NCAR (National Center for Atmospheric Research) reanalysis project began in 1991 to produce the past global analyses of atmospheric fields in support of the needs of the research and climate monitoring communities [*Kalany et al*., 1996; *Kistler et al*., 2001]. Based on a frozen state-of-the-art analysis/forecast system, data assimilation is performed using historical data from 1948 to the present [*Kalany et al*., 1996]. The Department of Energy (DOE) conducted a repetition of the reanalysis for the years from 1979 up to present in the Atmospheric Model Intercomparison Project (AMIP-II) to correct several human processing errors in the NCEP/NCAR reanalysis [*Kanamitsu et al*., 2002; *Vey et al*., 2010]. The NCEP/DOE AMIP-II Reanalysis (R-2) is generated using an improved physics model and more consistent observations [*Kanamitsu et al*., 2002]. In this study, the PWV data from the NCEP/DOE AMIP-II Reanalysis (R-2) (hereafter, simply referred to as NCEP reanalysis) covering the period 1979–2014 are used for the trend estimation. Like the ERA-Interim reanalysis data, the NCEP PWV data have a temporal coverage of 1979–2014 and a temporal resolution of 6 h. However, the spatial resolution of NCEP PWV is only $2.5° \times 2.5°$.

2.3. Radiosonde Observations

Radiosonde observations are the longest observational record of precipitable water vapor. Currently, there are more than 900 radiosonde stations globally, most of which, however, are located at developed countries [*Vey et al*., 2010]. Based on the balloon-borne platform, radiosondes can directly measure meteorological parameters including pressure, temperature, and relative humidity at various heights. PWV can be calculated from an integral of the meteorological profiles. In this study, quality-assured radiosonde data from the Integrated Global Radiosonde Archive (IGRA) are adopted to derive the global water vapor trends [*Durre et al*., 2006]. IGRA database includes records from more than 1500 radiosonde global stations with varying observation periods [*Durre et al*., 2006]. Radiosonde observations are estimated to measure the PWV with an accuracy of a few millimeters or even better [*Niell et al*., 2001; *Chen and Liu*, 2016]. *Chen and Liu* [2016] analyzed the uncertainty of water vapor estimation from radiosondes in China, and they showed that the uncertainties of the radiosonde-derived PWV are in the range of 0–1.5 mm. In the analysis of annual PWV time series for each station, we require at least 10 months of data be available for each year, and for each month at least 50% days of data be available [*Zhao et al*., 2012]. As a result, a total of 576 radiosonde stations meeting this data completeness requirement are selected for this study. Figure 1 shows the geographical distribution of the 576 radiosonde sites. It can be seen that most of the stations are located in the Northern Hemisphere, especially over Europe and America.

2.4. Global Positioning System

The International GNSS (Global Navigation Satellite System) Service (IGS) has operated a worldwide GNSS network with more than 400 permanent tracking stations since 1994 [*Beutler et al*., 1999]. The zenith

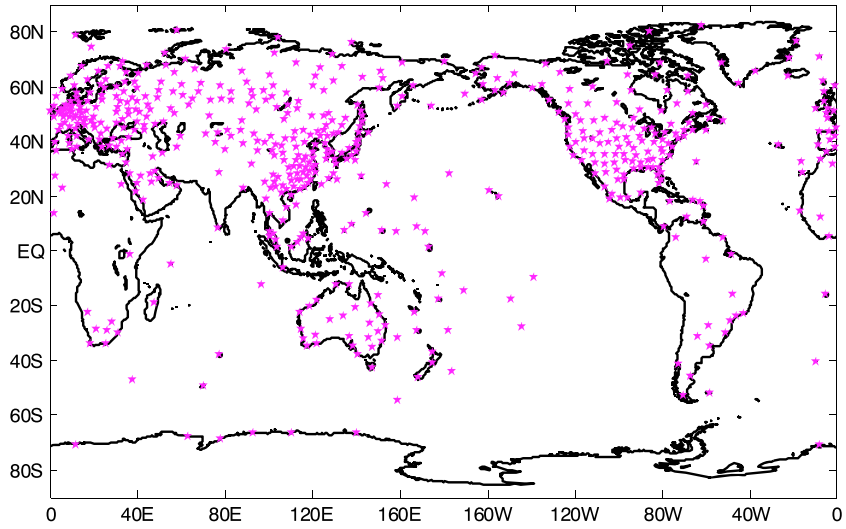

Figure 1. Geographical distribution of the 576 radiosonde stations selected for this study.

tropospheric delay (ZTD) products are retrieved from the GPS/GNSS observations and are provided regularly by the IGS [*Beutler et al.*, 1999]. ZTD is the sum of the zenith hydrostatic delay (ZHD) and the zenith wet delay (ZWD). To separate the ZWD from the ZTD, ZHD should be known and its value can usually be estimated from the empirical models with meteorological data as inputs. However, many IGS stations are not equipped with meteorological sensors and thus are unable to provide complete meteorological observations. Some IGS stations are equipped with meteorological sensors, but there are gaps in the meteorological observations due to equipment outage. *Chen and Liu* [2016] compared nine empirical ZHD models using data from China and found that ZHD derived from the ECMWF reanalysis data has the highest accuracy of 2.8 mm in China. The ECMWF reanalysis data are therefore employed to calculate the ZHD in this study. Then ZWD can be easily converted to PWV using a conversion factor which is a function of the mean temperature of the troposphere [*Bevis et al.*, 1994]. The accuracy of the GPS-inferred PWV based on numerous studies is likely to be 1–2 mm. [*Duan et al.*, 1996; *Elgered et al.*, 1997; *Niell et al.*, 2001; *Ning et al.*, 2011; *Lee et al.*, 2013].

The ZTD products used in this study are retrieved from the IGS Tide Gauge Benchmark Monitoring-Working Group (TIGA-WG) data reprocessing campaign that was carried out at the German Research Centre for Geosciences (GFZ) [*Deng et al.*, 2015]. This campaign aims to reanalyze the GPS data collected by the IGS global network since 1994 in a fully consistent way using the latest models and methodology. Therefore, compared with the official IGS ZTD products, the reprocessed ZTD products are more coherent and more reliable for the water vapor trend study. The mean uncertainty of the ZTD product is about 4 mm [*Li et al.*, 2012]. By taking the accuracy of 2.8 mm of ECMWF-derived ZHD in China into account and performing the error propagation of ZWD = ZTD − ZHD, the uncertainty of ZWD is about 5 mm. This implies that the PWV error is smaller than 1 mm if the ZWD is converted into PWV data. In this paper, 15 year GPS PWV data from global GPS stations for the period 2000–2014 are adopted to validate the global water vapor trends estimated from the reanalysis data. For each station, the annual PWV is calculated if at least 10 months of data are available for this year, while for each month at least 50% days of data are required. In this study, 100 stations meet this data selection requirement and they are shown in Figure 2.

2.5. Microwave Satellite

Based on the satellite-borne passive microwave detectors, it is possible to observe the atmospheric water vapor over the vast oceanic regions where only limited ship-based and buoy-based observations were previously available [*Andersson et al.*, 2010]. Unlike the infrared measurements, passive microwave detectors are able to measure the atmospheric water vapor content under both cloud-free and cloudy conditions since microwaves can penetrate clouds. Based on homogenized observations of the Special Sensor

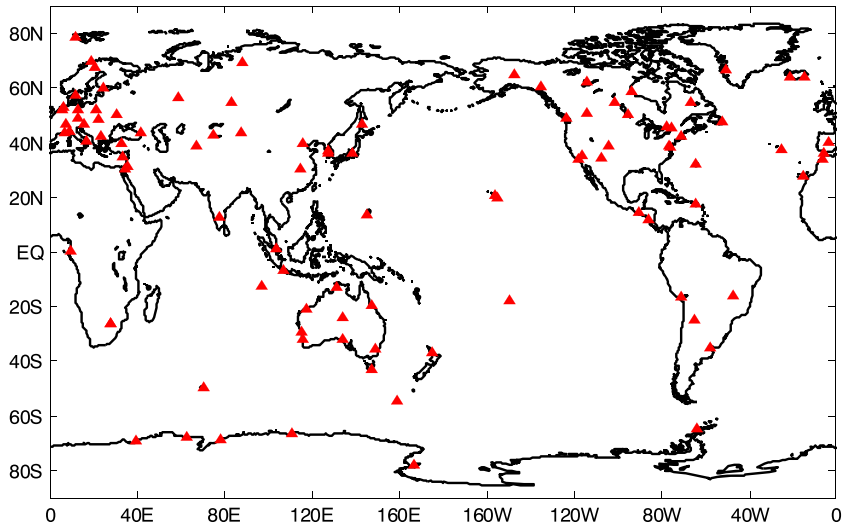

Figure 2. Distribution of the 100 selected IGS stations in this study.

Microwave/Imager (SSM/I) over the ice-free global ocean, Satellite Application Facility on Climate Monitoring (CMSAF) of European Organization for the Exploitation of Meteorological Satellites (EUMETSAT) provides long-term satellite-derived PWV data records [*Schröder et al.*, 2013; *Mieruch et al.*, 2014]. The latest Hamburg Ocean Atmosphere Parameters and Fluxes from Satellite Data (HOAPS) version 3.2 PWV data set covers the period from July 1987 to December 2008 with a spatial resolution of 0.5°×0.5° and is freely available at http://www.cmsaf.eu/ [*Fennig et al.*, 2012]. The assessment of the HOAPS PWV data has shown good agreements with data sets from the Advanced Television and Infrared Observation Satellite Operational Vertical Sounder (ATOVS) and reanalysis model with root-mean-square (RMS) errors of less than 2 mm [*Jonas et al.*, 2009].

Since no data are provided by HOAPS after 2008, CMSAF ATOVS PWV data set derived from the ATOVS observations is exploited to extend the PWV data set to the year of 2014. The ATOVS is composed of Advanced Microwave Sounding Unit (AMSU) and High-Resolution Infrared Sounder (HIRS)/3 which is flying on board the National Oceanic and Atmospheric Agency (NOAA) satellites, NOAA 15, NOAA 16, NOAA 17, NOAA 18, and NOAA 19, and on board the European Metop-A satellite [*Li et al.*, 2000; *Courcoux and Schröder*, 2013]. The CMSAF ATOVS data set provides PWV products over both land and ocean with a spatial resolution of 0.5°×0.5°. In this study, only the ocean data from January 2009 to December 2014 are used. The accuracies of the CMSAF ATOVS PWV data are about 2–4 mm when evaluated by water vapor observations from radiosonde and Atmospheric Infrared Sounder (AIRS) satellites [*Courcoux and Schröder*, 2013].

In the trend analysis, the temporal inhomogeneity in the PWV data between HOAPS and ATOVS should be carefully examined. Therefore, a homogeneity detection is performed for each grid point. In the detection, 6 year (2003–2008) monthly mean PWV data from HOAPS are compared with the following 6 year (2009–2014) data from ATOVS. First, PWV time series from HOAPS and ATOVS are detrended. Then Student's *t* test is performed to examine the hypothesis that mean value of detrended HOAPS PWV data has no significant difference from that of ATOVS. If the hypothesis is rejected, the PWV data for this point are regarded to be inhomogeneous and will be excluded from the data set.

2.6. Method for Trend Estimation

Global water vapor trends are estimated using annually averaged PWV time series data. The linear regression method is exploited to estimate the trends [*Zhai and Eskridge*, 1997]:

$$y(t) = a + bx \tag{1}$$

where y is the PWV data time series (unit: mm) and x is the corresponding time (unit: year); b represents the annual global water vapor trend (unit: mm/yr). The terms a (unit: mm) and b can be estimated from [*Zhai and Eskridge*, 1997]:

$$a = \frac{1}{n}\sum_{i=1}^{n} y_i - \left(\frac{1}{n}\sum_{n=1}^{n} x_i\right) b \tag{2}$$

$$b = \frac{S_{xy}}{S_{xx}} \tag{3}$$

$$S_{xx} = \sum_{i=1}^{n} x_i^2 - \frac{1}{n}\left(\sum_{i=1}^{n} x_i\right)^2 \tag{4}$$

$$S_{xy} = \sum_{i=1}^{n} x_i y_i - \frac{1}{n}\left(\sum_{i=1}^{n} x_i\right)\left(\sum_{i=1}^{n} y_i\right) \tag{5}$$

where n is the total number of years in study. The estimation error of the trend b is given by

$$\sigma_b = \sqrt{\frac{S_{yy} - bS_{xy}}{S_{xx}(n-2)}} \tag{6}$$

$$S_{yy} = \sum_{i=1}^{n} y_i^2 - \frac{1}{n}\left(\sum_{i=1}^{n} y_i\right)^2 \tag{7}$$

In this study, the uncertainty of the estimated trend is given as 2 times the standard deviation ("2 sigma") with a confidence probability of 95.5%.

The amount of atmospheric water vapor varies greatly from region to region; thus, the percentage trend P_b (unit: % decade^{-1}) is defined in this study for a more intuitional understanding of water vapor change [*Zhai and Eskridge*, 1997]:

$$P_b = 1000 \cdot \frac{b}{\bar{y}} \tag{8}$$

where $\bar{y}$ is the annual average of PWV (unit: mm). The Student's t test is performed to examine the significance level of the trend estimates. The statements for the hypothesis test are expressed as

$$H_0 : b = 0, \quad H_1 : b \neq 0 \tag{9}$$

The null hypothesis H_0 states that the trend is equal to 0, and the alternative hypothesis H_1 states that the trend is not equal to 0. The test statistic is calculated by

$$T_0 = \frac{|b| \cdot \sqrt{S_{xx}}}{\sqrt{\frac{S_{yy} - bS_{xy}}{n-2}}} \tag{10}$$

The test statistic, T_0, follows a distribution with $(n-2)$ degrees of freedom. The acceptance region for the null hypothesis H_0 is

$$-t_{\alpha/2,n-2} < T_0 < t_{\alpha/2,n-2} \tag{11}$$

where α is the significance level (0.05 used in this study). $t_{\alpha/2,n-2}$ and $-t_{\alpha/2,n-2}$ are the critical values for the two-sided hypothesis. The term $t_{\alpha/2,n-2}$ is the percentile of the t distribution corresponding to a cumulative probability of $1-\alpha/2$. If the null hypothesis is accepted, it indicates that no linear relationship exists between x and y. In the case when the null hypothesis is rejected, the linear model is sufficient to imply that the estimated trend is significant.

3. Validation of PWV From ECMWF and NCEP by Radiosonde, GPS, and Microwave Satellite Observations

The use of reanalysis data in trend estimation requires exact knowledge of the accuracy of the PWVs derived from the models. As discussed above, the radiosonde, GPS, and microwave satellite can measure

Table 1. Statistical Results for the Validation of PWV Derived From ECMWF (1979–2014) and NCEP (1979–2014) by Radiosonde (1979–2014), GPS (2000–2014), and Microwave Satellite (1992–2014)[a]

Comparison	Coverage	Bias (mm)	RMS (mm)
Radiosonde versus ECMWF	Global	0.37	2.88 (15.8%)
	Tropical	0.68	4.47 (11.7%)
	Temperate	0.28	2.65 (16.5%)
	Polar	0.06	1.05 (14.6%)
Radiosonde versus NCEP	Global	0.28	3.12 (17.1%)
	Tropical	0.13	5.07 (13.3%)
	Temperate	0.33	2.48 (15.4%)
	Polar	0.03	1.03 (14.3%)
GPS versus ECMWF	Global	0.01	3.43 (19.5%)
	Tropical	0.47	3.82 (11.1%)
	Temperate	0.01	3.38 (22.2%)
	Polar	−0.70	3.11 (43.1%)
GPS versus NCEP	Global	−0.06	4.13 (23.5%)
	Tropical	−0.32	5.84 (17.0%)
	Temperate	0.09	3.80 (25.0%)
	Polar	−0.86	3.30 (45.7%)
Satellite versus ECMWF	Global	0.10	1.65 (6.9%)
	Tropical	0.85	2.01 (5.1%)
	Temperate	−0.35	1.49 (8.9%)
Satellite versus NCEP	Global	−0.78	3.84 (16.0%)
	Tropical	1.19	5.15 (12.9%)
	Temperate	−2.03	3.07 (18.3%)

[a]Values in the parentheses are relative RMS errors.

the atmospheric water vapor content with high accuracy of several millimeters. Therefore, a validation study is carried out to evaluate the ECMWF and NCEP-derived PWV using radiosonde, GPS, and satellite observations, allowing a reliable interpretation of the quality of the reanalysis data. ECMWF and NCEP data are interpolated onto the radiosonde/GPS sites to derive the PWV data and then are directly compared with PWV measured at the local station. Radiosonde and GPS sites are classified into three groups: tropical region (23.5°S–23.5°N), temperate region (23.5°S–66.5°S and 23.5°N–66.5°N), and polar region (66.5°S–90°S and 66.5°N–90°N). In addition to the global accuracy, performances of the reanalysis data are also evaluated in these three regions.

Table 1 gives the bias and RMS error of the differences between ECMWF/NCEP-derived PWVs and radiosonde/GPS/satellite-measured PWVs. In the evaluation by radiosonde, ECMWF gets a smaller RMS error of 2.88 mm than that of NCEP with a value of 3.12 mm. The lower global accuracy of the NCEP is attributed to the poor performance in the tropical region. As seen in Table 1, the RMS errors in the tropical region for NCEP and ECMWF are 5.07 and 4.47 mm, respectively. For the temperate and polar regions, however, NCEP shows slightly better performance than ECMWF. Figure 3 presents the changes of bias and RMS error with year. After the year of 2009, RMS errors for both reanalyses show a persistent decrease (see Figures 3a and 3b). NCEP has larger RMS errors, but its biases are smaller than ECMWF.

In the evaluation by GPS, RMS errors for both ECMWF and NCEP are larger than those with radiosonde. This can be explicable by the fact that radiosonde observations are already assimilated to the reanalysis models [*Vey et al.*, 2010]. Therefore, better agreements are found in the comparison between reanalysis model and radiosonde. GPS-observed water vapor can be used as an independent data source to evaluate the reanalysis data. In the evaluation by GPS, ECMWF and NCEP obtain RMS errors of 3.43 and 4.13 mm, respectively. ECMWF consistently shows better agreement with GPS than the NCEP in the three climatic regions. For the three climatic zones, it is noteworthy that both ECMWF and NCEP get poor performance in the polar region. The ECMWF and NCEP have relative RMS errors, which are defined as the ratio of RMS error to observation, of 43.1% and 45.7%, respectively. They are about 3 times the ones obtained from the comparisons with radiosonde. In other words, it reveals the poor performance of the reanalysis model in the polar region since few observations in this region are available for data assimilation. For the comparison in each year, as shown in Figures 3c and 3d, their RMS errors are steady without large fluctuations and their biases are very small and approach 0.

As seen in Figures 1 and 2, most of the radiosonde and GPS stations are located on continents; thus, the above evaluation is valid on land only. To assess the performance of reanalysis models over the vast oceanic region, a further evaluation is carried out using PWV data from microwave satellites. The RMS errors yielded for ECMWF and NCEP are 1.65 mm and 3.85 mm, respectively. The rather good agreement between the ECMWF and satellite is probably because the assimilation of clear-sky radiances measured by satellite onboard radiometers into the ECMWF model [*Dee et al.*, 2011]. For NCEP, however, the satellite radiances

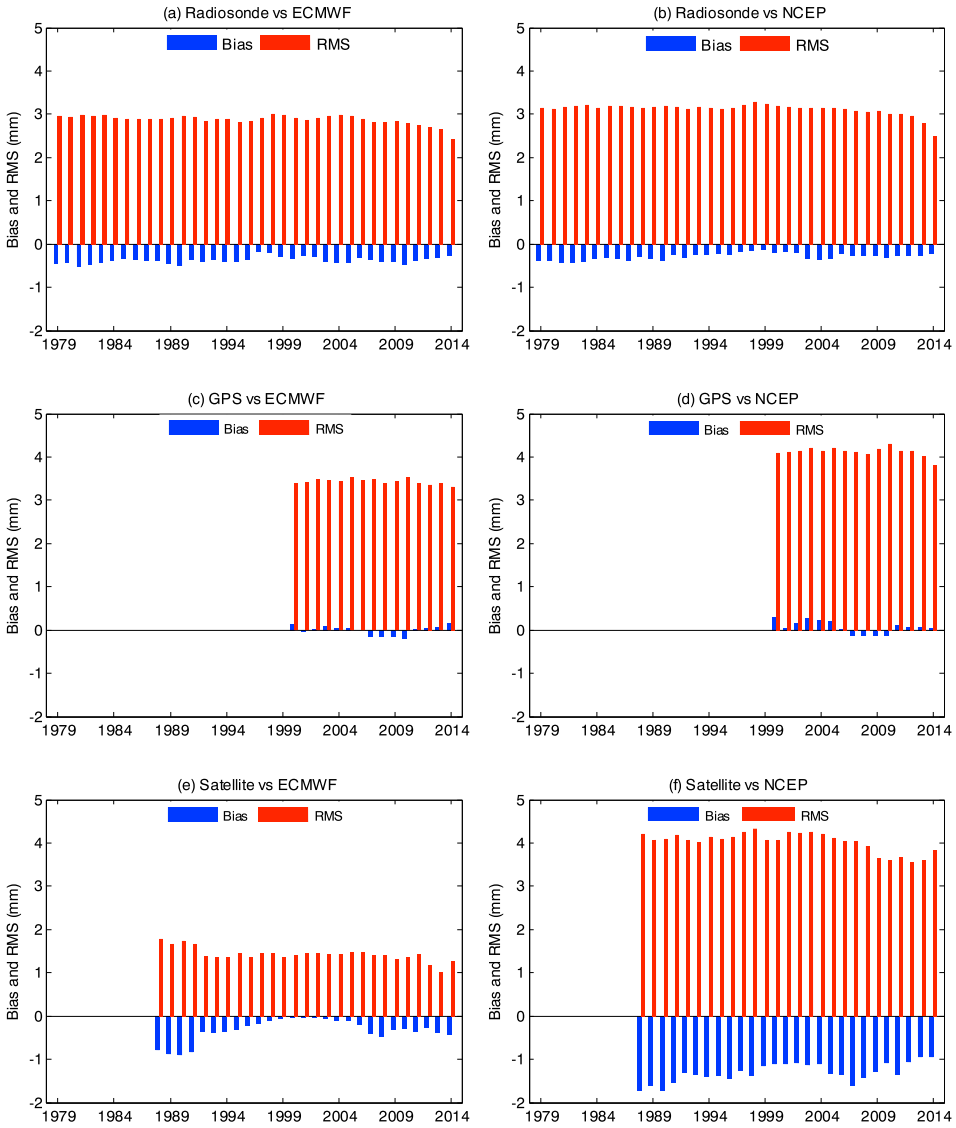

Figure 3. Bias and RMS error of PWV differences between (a) radiosonde and ECMWF, (b) radiosonde and NCEP, (c) GPS and ECMWF, (d) GPS and NCEP, (e) satellite and ECMWF, and (f) satellite and NCEP for each year.

are not employed and can be incorporated to get a better performance [*Kanamitsu et al.*, 2002]. For the climatic zones, relative RMS errors obtained by NCEP are 2.5 and 2.1 times larger than those of ECMWF for tropical and temperate region, respectively. In Figure 3e, it can be seen that there is an obvious shift in bias from 1991 to 1992, but this shift is inexistent in Figure 3f for NCEP. This shift will have a large impact on the trend estimation from ECMWF.

The correlation coefficients of PWV between reanalysis models and radiosonde/GPS are calculated at each station as shown in Figure 4. Higher correlation coefficient implies more similar PWV trends can be obtained from the two data sets. In Figures 4a and 4b, high correlation coefficients ($>$0.9) between radiosonde and reanalysis are observed at most Eurasia and North America stations. ECMWF and radiosonde show strong correlation with the smallest correlation coefficient larger than 0.6 at a tropical station. Radiosonde and NCEP correlation is relatively low at most tropical stations with correlation coefficients ranging from 0.3 to 0.8. For GPS and ECMWF/NCEP, strong correlation is shown at most stations in Eurasia, North America, and Australia. However, in the Antarctic, weak correlations ($<$0.6) are found for both GPS-ECMWF and GPS-NCEP.

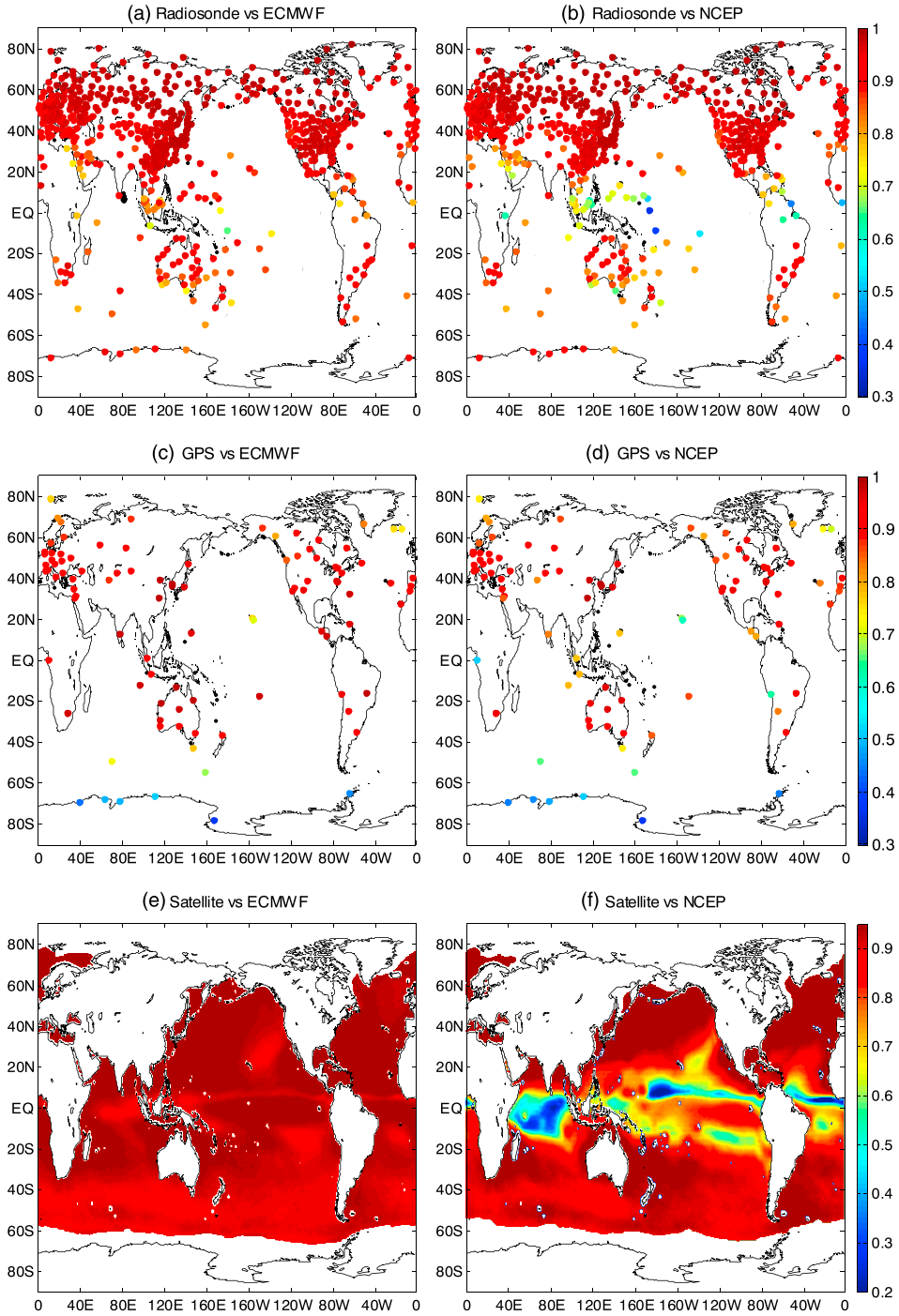

Figure 4. Map of correlation coefficient between two sets of PWV data: (a) radiosonde and ECMWF, (b) radiosonde and NCEP, (c) GPS and ECMWF, (d) GPS and NCEP, (e) satellite and ECMWF, and (f) satellite and NCEP. Correlation coefficients in Figures 4a and 4b are calculated for the period 1979–2014, Figures 4c and 4d for the period 2000–2014, and Figures 4e and 4f for the period 1992–2014.

In addition to radiosonde and GPS, the correlation coefficients of PWV between satellite and ECMWF, and satellite and NCEP are presented in Figures 4e and 4f, respectively. The satellite-ECMWF correlation (>0.8) is strong over the global ocean. For the relationship between satellite and NCEP, low correlation coefficients are observed over most tropical oceans. Especially for tropical Indian Ocean and tropical Pacific Ocean, very low correlation (<0.3) is found in a wide range of ocean.

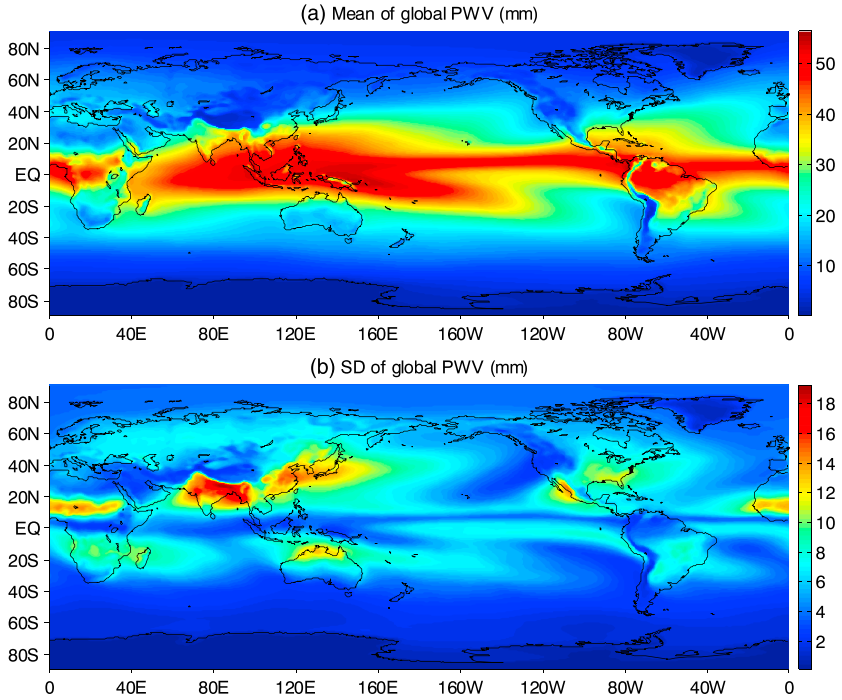

Figure 5. (a) Means and (b) SDs of the global PWV derived from the ERA-Interim reanalysis for the 36 year period of 1979–2014. SD represents the seasonal variability of the global PWV.

4. Results and Discussion

4.1. Distribution and Variability of Global Water Vapor

As shown in section 3, the performance of ECMWF PWV data is better than that of NCEP; thus, the ECMWF is used to study the distribution and variability of global water vapor. Figure 5 shows the spatial distribution of global mean PWVs derived from the 36 year ERA-Interim reanalysis. Their standard deviations (SD) are also calculated to show the seasonal variability of global water vapor. The global mean PWV varies in the range of 0–55 mm depending upon the region. Larger mean PWVs occur in the tropical regions particularly in the west Pacific and east Indian Ocean regions. For the polar and some high terrain regions (e.g., Tibetan Plateau), the mean PWV values are very small ranging from several millimeters to merely a fraction of 1 mm. Figure 5b shows that water vapor has larger variations over land than over ocean. In the equatorial regions, water vapor keeps at a high level all year round and PWV has little variation. For the Antarctic, high terrain and desert regions, water vapor variability is small due to the extremely dry atmosphere in these regions. In addition, it can be observed that larger variations of water vapor occur in South Asia, East Asia, Sahel, west Mexico, and north Australia. The south foothill of Himalayas has the largest PWV variation with a SD ~18 mm. This is attributed to the monsoon climate that results in large changes in precipitation at different seasons in these regions.

The maps of seasonal global mean PWV for the four seasons DJF, MAM, JJA, and SON are shown in Figure 6. It shows that the mean PWV is ~40–65 mm over most equatorial areas with relatively small seasonal variations (≤5 mm). For the North Hemisphere, summer (JJA) has significantly higher PWV than other seasons, whereas it is not obvious for the South Hemisphere (summer is DJF) because of the large oceanic coverage in the Southern Hemisphere. Large water vapor variations can be found to occur mainly in two transition seasons MAM and SON.

4.2. Trends in Global Water Vapor

Figure 7 shows the 1979–2014 time series of ECMWF and NCEP annual PWV averaged over global, tropical, temperate, and polar regions. Linear regression analysis is performed for each region, and the estimated linear trends are listed in Table 2. In addition, PWV trends are also estimated separately over land and ocean

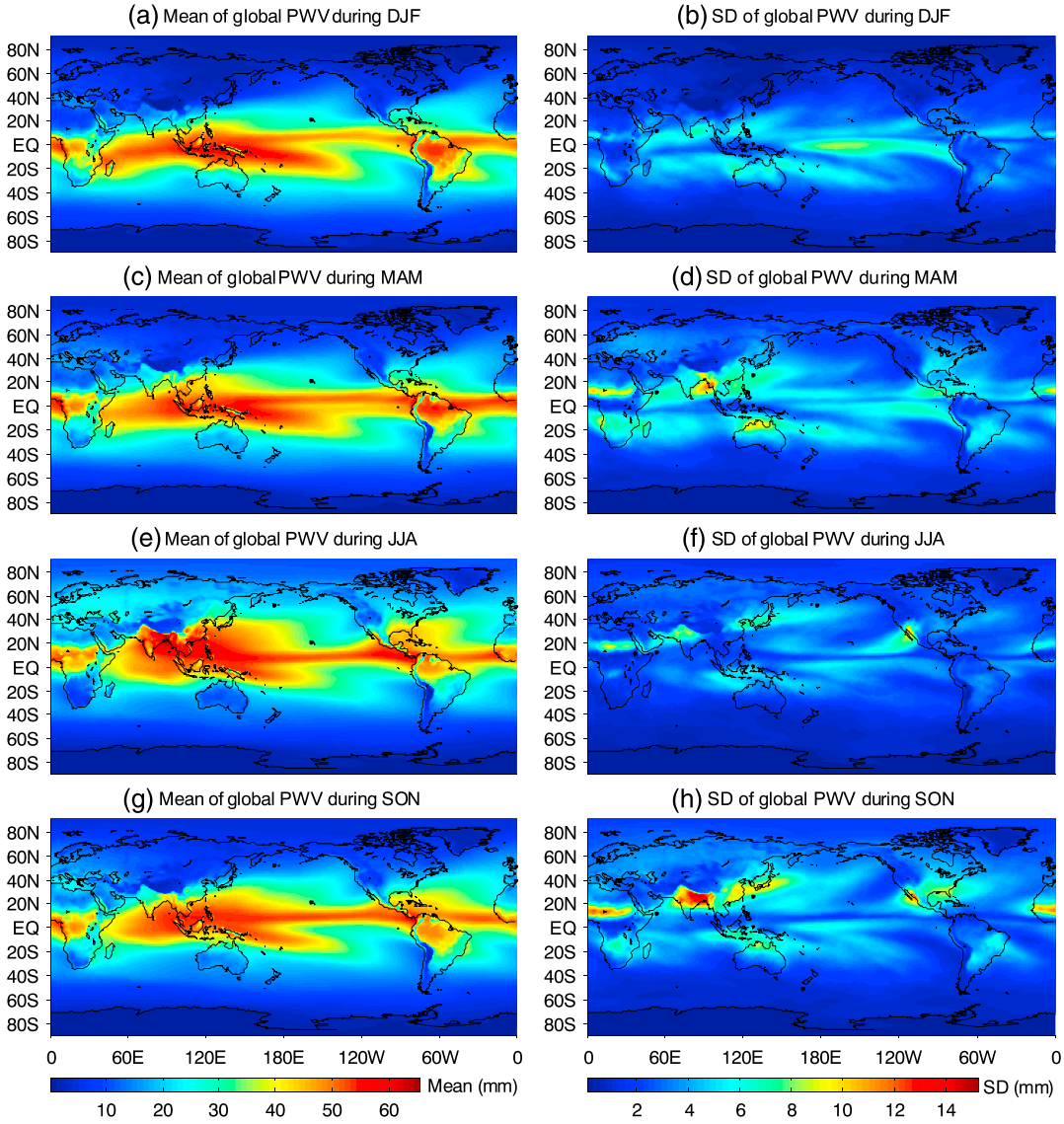

Figure 6. (a, c, e, g) Means and (b, d, f, h) SDs of global PWV derived from the 36 year (1979–2014) ERA-Interim reanalysis for different seasons. SD represents the interannual variability of the global PWV for the four seasons.

for ECMWF and NCEP. Figure 8 exhibits the spatial distributions of linear trends, expressed as percentages, of atmospheric water vapor.

Table 2 shows that the PWV variation trends estimated from ERA-Interim reanalysis over the period 1979–2014 for global, tropical, temperate, and polar regions are all positive, with a rate of $0.17 \pm 0.35\%\,\text{decade}^{-1}$, $0.02 \pm 0.37\%\,\text{decade}^{-1}$, $0.14 \pm 0.31\%\,\text{decade}^{-1}$, and $1.77 \pm 0.85\%\,\text{decade}^{-1}$, respectively. In the tropical and temperate regions, the estimated PWV trends are not significant and have a high uncertainty. The polar region observes the largest trend, suggesting that the polar region has undergone a significant increase in water vapor. This is probably due to global warming [*IPCC*, 2015]. If considering the Arctic and Antarctic separately, Figure 8a illustrates that the Arctic has undergone an increase of $2.98 \pm 1.21\%\,\text{decade}^{-1}$ in PWV, whereas a downward trend of $-2.03 \pm 1.34\%\,\text{decade}^{-1}$ is observed in the Antarctic. This opposite change at the north and south polar regions is consistent with temperature studies suggesting that the Arctic is warming faster than the global average [*Screen et al.*, 2012; *Walsh*, 2014]. However, the Antarctic climate change is still debatable [*Guglielmin and Cannone*, 2012] as both warming [*Turner et al.*, 2007] and cooling trends [*Doran et al.*, 2002] have been observed in the Antarctic region. Trend estimation is also carried out

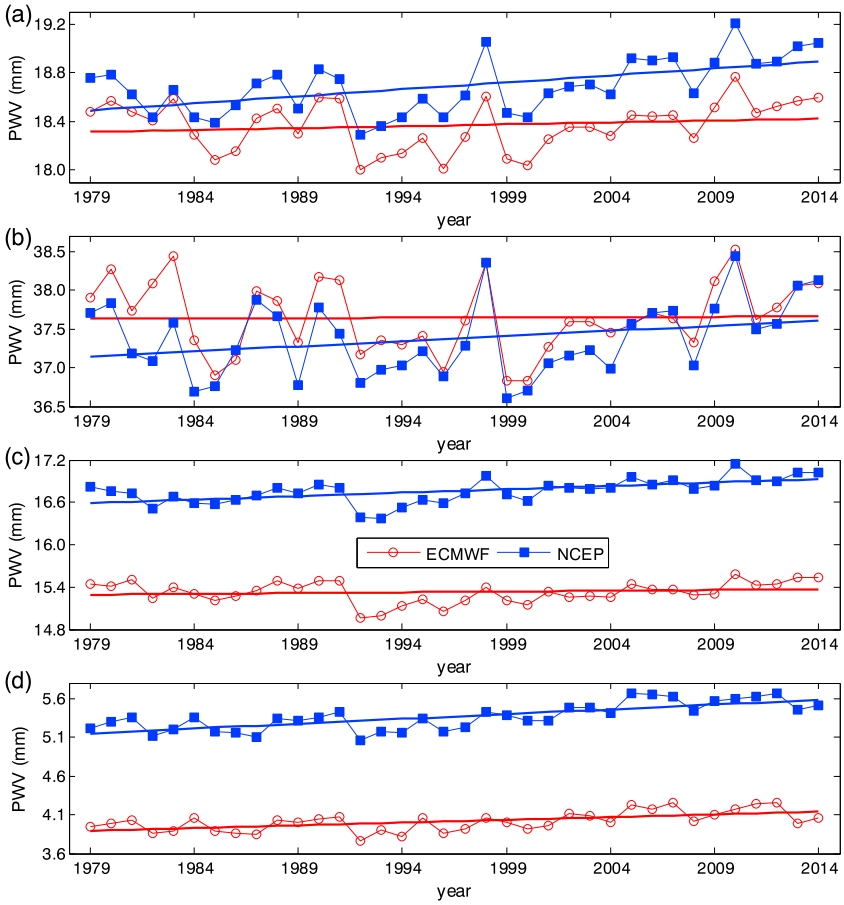

Figure 7. ECMWF and NCEP PWV time series averaged over (a) global, (b) tropical, (c) temperate, and (d) polar regions during the period 1979–2014.

separately over land and ocean, yielding a significant trend of $0.45 \pm 0.39\%$ decade^{-1} and a nonsignificant trend of $0.07 \pm 0.39\%$ decade^{-1}, respectively. It is surprising that ECMWF produces a near-zero trend of global PWV, especially over the ocean. The near-zero trend is inconsistent with the positive trend of the global surface temperature [*Fyfe et al.*, 2016] and also the moistening trend in the upper troposphere over this period [*Chung et al.*, 2014]. This is probably attributed to the overestimation of PWV over the ocean by ECMWF for the years before 1992. As seen in Figure 3e, PWV biases between microwave satellite and ECMWF for years 1988–1991 are evidently greater than those from 1992 onward. This bias shift is due to changes in observations from SSM/I as new satellites came online with an ability to retrieve PWV from rain-affected radiances [*Trenberth et al.*, 2011; *Lorenz and Kunstmann*, 2012]. Due to the limited temporal coverage of the HOAPS data set, it is unable to examine the ECMWF PWV over the ocean before 1988. In addition, as shown in Figure 7a, there is a bias between the global annual PWV series from ECMWF and NCEP from 1985 onward. Before 1985, ECMWF PWV series agree well with that of NCEP. The near-zero trend derived from ECMWF is thus very likely related to the overestimation of PWV before 1992. Thus, the ECMWF-derived PWV trends for the period 1979–2014 are likely unreliable.

In Figure 7, an abrupt PWV decrease is observed during 1991–1992. This abrupt change is likely related to the eruption of Mount Pinatubo in 1991 [*Trenberth and Smith*, 2005]. *Soden et al.* [2002] reported that the volcanic aerosols reduced the solar heating, which led to a global cooling associated with a decrease in global PWV by an order of 0.5 mm. In addition, as discussed above, ECMWF overestimates the PWV before 1992. For this reason, the trend for the period 1992–2014 (after the year of 1991) is separately estimated. In Table 2, a statistically significant global increase trend of $1.31 \pm 0.47\%$ decade^{-1} is exhibited. For the three climatic zones, the polar region shows the largest upward trend of $3.62 \pm 1.59\%$ decade^{-1}, followed

Table 2. PWV Change Trends Estimated for Different Regions Over Three Periods (Unit: mm Decade^{-1})[a]

		Trend		
Data Source	Coverage	1979–2014	1992–2014	2000–2014
ECMWF	Global	0.03 ± 0.06 (0.17 ± 0.35%)	*0.24 ± 0.08 (1.31 ± 0.47%)*	*0.31 ± 0.13 (1.66 ± 0.73%)*
	Tropical	0.01 ± 0.15 (0.02 ± 0.37%)	*0.38 ± 0.23 (1.01 ± 0.62%)*	*0.66 ± 0.34 (1.75 ± 0.92%)*
	Temperate	0.02 ± 0.05 (0.14 ± 0.31%)	*0.21 ± 0.05 (1.38 ± 0.35%)*	*0.22 ± 0.09 (1.42 ± 0.60%)*
	Polar	*0.07 ± 0.03 (1.77 ± 0.85%)*	*0.15 ± 0.06 (3.62 ± 1.59%)*	0.09 ± 0.13 (2.27 ± 3.22%)
	Land	*0.07 ± 0.06 (0.45 ± 0.39%)*	*0.17 ± 0.12 (1.13 ± 0.79%)*	*0.24 ± 0.18 (1.53 ± 1.18%)*
	Ocean	0.01 ± 0.07 (0.07 ± 0.39%)	*0.28 ± 0.08 (1.41 ± 0.43%)*	*0.34 ± 0.14 (1.72 ± 0.72%)*
NCEP	Global	*0.11 ± 0.06 (0.61 ± 0.33%)*	*0.30 ± 0.10 (1.58 ± 0.53%)*	*0.35 ± 0.16 (1.84 ± 0.85%)*
	Tropical	0.13 ± 0.15 (0.35 ± 0.40%)	*0.47 ± 0.26 (1.27 ± 0.70%)*	*0.83 ± 0.38 (2.21 ± 1.02%)*
	Temperate	*0.10 ± 0.04 (0.58 ± 0.27%)*	*0.24 ± 0.07 (1.44 ± 0.42%)*	*0.20 ± 0.11 (1.19 ± 0.65%)*
	Polar	*0.12 ± 0.04 (2.30 ± 0.71%)*	*0.22 ± 0.06 (4.05 ± 1.20%)*	0.14 ± 0.13 (2.52 ± 2.35%)
	Land	*0.15 ± 0.07 (1.02 ± 0.46%)*	*0.35 ± 0.12 (2.32 ± 0.84%)*	*0.48 ± 0.19 (3.15 ± 1.26%)*
	Ocean	*0.09 ± 0.06 (0.44 ± 0.30%)*	*0.26 ± 0.10 (1.26 ± 0.47%)*	*0.27 ± 0.18 (1.27 ± 0.86%)*
Radiosonde	Global	*0.11 ± 0.05 (0.57 ± 0.28%)*	*0.32 ± 0.22 (1.67 ± 1.17%)*	*0.34 ± 0.26 (1.78 ± 1.34%)*
	Tropical	0.20 ± 0.38 (0.53 ± 1.03%)	*0.39 ± 0.21 (1.04 ± 0.58%)*	*0.73 ± 0.27 (1.96 ± 0.73%)*
	Temperate	0.04 ± 0.12 (0.21 ± 0.64%)	*0.26 ± 0.18 (1.47 ± 1.08%)*	0.21 ± 0.22 (1.23 ± 1.29%)
	Polar	0.09 ± 0.13 (1.13 ± 1.65%)	*0.32 ± 0.12 (4.10 ± 1.57%)*	0.08 ± 0.14 (1.04 ± 1.87%)
GPS	Global	--	--	0.22 ± 0.28 (1.29 ± 1.66%)
	Tropical	--	--	0.23 ± 0.72 (0.69 ± 2.15%)
	Temperate	--	--	*0.22 ± 0.12 (1.46 ± 0.78%)*
	Polar	--	--	0.24 ± 0.33 (3.55 ± 4.93%)
Satellite	Ocean	--	*0.32 ± 0.16 (1.52 ± 0.61%)*	*0.34 ± 0.10 (1.62 ± 0.47%)*

[a]Values in the parentheses are the relative trends (unit: % decade^{-1}). The trends presented in italics indicate that they are statistically significant at the 95% confidence level.

by an increase trend of 1.38 ± 0.35% decade^{-1} and 1.01 ± 0.62% decade^{-1} over the temperate and tropical regions, respectively. Over the ocean, a significant PWV increase is observed which is larger than that over the land. Similarly, due to the impact of 1997–1998 ENSO event, the PWV trends for the period 2000–2014 are separately estimated.

As shown in Figure 7 and Table 2, in the period 2000–2014, the global PWV upward trend becomes much larger than those of periods 1979–2014 and 1992–2014. The increase trends are more apparent in the tropical (1.75 ± 0.92% decade^{-1}) and temperate (1.42 ± 0.60% decade^{-1}) regions. The polar region's increase trend is slightly smaller than that in the 1992–2014 period. However, it is still as high as 2.27 ± 3.22% decade^{-1}. If we examine Figures 8b and 8c, it can be found that the Arctic and Antarctic have distinct PWV change trends. PWV increase trends of 0–10% decade^{-1} are widespread over the Arctic region, but negative trends (−15–0% decade^{-1}) are observed over the Antarctic region in the past two decades. Moreover, evident decrease trends are also found over the Asian continent, United States, and North Africa over the past two decades. In addition to the Arctic, large positive PWV trends (0 ~ 15% decade^{-1}) are found over the north and west Pacific, Europe, eastern Indian Ocean, and southern Asia.

Table 2 also summarizes the PWV trends derived from NCEP. Statistically significant global PWV trends are 0.61 ± 0.33% decade^{-1}, 1.58 ± 0.53% decade^{-1}, and 1.84 ± 0.85% decade^{-1} for the periods 1979–2014, 1992–2014, and 2000–2014, respectively. Consistent with the ECMWF results, the polar region is observed to have the largest positive PWV trends for all the three periods. The PWV trends derived from NCEP are basically consistent with those from the ECMWF for the periods 1992–2014 and 2000–2014. As shown in Figure 7 a, the PWV trends from ECMWF and NCEP are very consistent after 1992. Similar trends are captured by ECMWF and NCEP in the temperate and polar regions though obvious shifts exist. Globally, NCEP PWV trend estimates are larger than the ECMWF ones. The higher NCEP PWV trend is attributed to the much larger estimation over land, which is twice larger than that from ECMWF. For the period 1979–2014, the much smaller global trend from ECMWF is also because of the effects of PWV overestimation before 1992. Over the ocean, NCEP-derived trend is smaller than that from ECMWF except for the period 1979–2014. The evaluation analysis in section 3 has shown that NCEP has a poorer performance especially in the tropical ocean; thus, the NCEP estimated trends are not as reliable as ECMWF. In addition, the PWV trends from radiosonde, GPS,

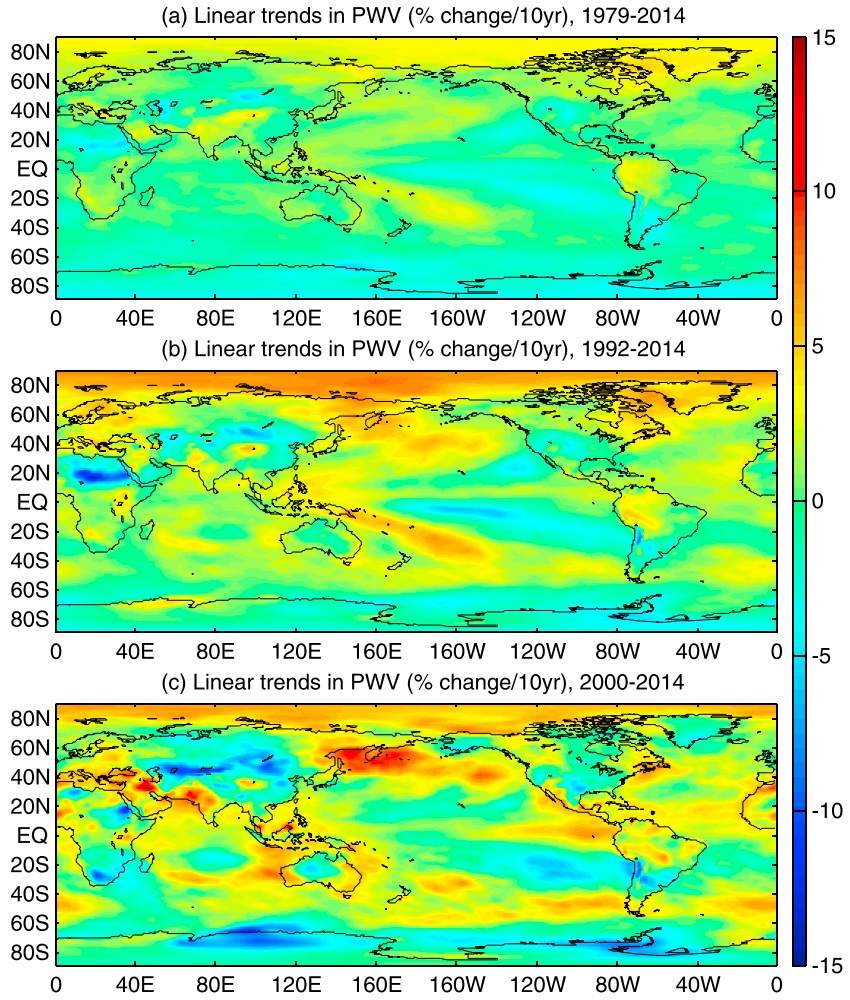

Figure 8. Spatial distributions of linear trends from the ECMWF PWV for the three periods: (a) 1979–2014, (b) 1992–2014, and (c) 2000–2014.

and microwave satellite data are also summarized in Table 2. Positive PWV trends of $1.52 \pm 0.61\%$ and $1.62 \pm 0.47\%$ decade^{-1} over the ocean for the two periods 1992–2014 and 2000–2014 are derived from the microwave satellite observations. The satellite-observed PWV trends are closer to those derived from ECMWF, consistent with the very good agreement of these two data sets demonstrated in Figure 4e.

Table 2 shows that global PWVs from the radiosonde have significant increase trends of $0.57 \pm 0.28\%$ decade^{-1}, $1.67 \pm 1.17\%$ decade^{-1}, and $1.78 \pm 1.34\%$ decade^{-1} for the periods 1979–2014, 1992–2014, and 2000–2014, respectively. In terms of three climatic regions, the polar region shows the largest increase trends for periods except 2000–2014, which are consistent with ECMWF and NCEP. In the tropical region, radiosonde-derived trends are larger than ECMWF but smaller than NCEP for the periods 1992–2014 and 2000–2014. For the temperate region, radiosonde-derived PWV trends are close to those estimated from ECMWF and NCEP. This may be because 79% of the 576 selected radiosonde stations are concentrated in the temperate region. In section 3, we have shown that ECMWF-derived PWV data have a high correlation with radiosonde measured PWV. The discrepancies in PWV trends are largely due to the different spatial coverage of the two data sets. In order to validate this speculation, ECMWF data are interpolated onto the radiosonde sites to get another set of PWV change trends. Global trends of 0.48% decade^{-1}, 1.60% decade^{-1}, and 1.73% decade^{-1} are obtained for the periods 1979–2014, 1992–2014, and 2000–2014, respectively, which are much closer to the radiosonde observed trends. In general, the radiosonde-derived PWV uptrends are greater than those from the ECMWF and NCEP.

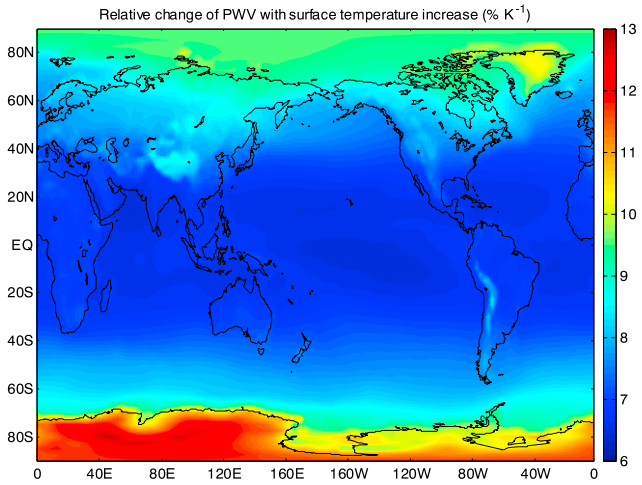

Figure 9. Relative changes of global PWV for 1 K rise in temperature (unit: % K^{-1}) according to the Clausius-Clapeyron equation. In the simulation, global surface temperature, temperature lapse rate, and relative humidity profile are derived by averaging the 36 year data from the ECMWF ERA-Interim reanalysis.

In Table 2, GPS-derived PWV trends only for the period 2000–2014 are shown due to the unavailability of enough GPS PWV data prior to 2000. The GPS PWV shows a nonsignificant global trend of 1.29 ± 1.66% $decade^{-1}$ that is smaller than the trends of 1.66 ± 0.73% $decade^{-1}$ and 1.84 ± 0.85% $decade^{-1}$ from the ECMWF and NCEP reanalyses, respectively, over the same period 2000–2014. In the tropical region, the GPS estimated trend (0.69 ± 2.15% $decade^{-1}$) is significantly smaller than those from ECMWF (1.75 ± 0.92% $decade^{-1}$) and NCEP (2.21 ± 1.02% $decade^{-1}$). However, in the polar region, a stronger increase trend (3.55 ± 4.93% $decade^{-1}$) is observed by GPS compared with PWV trends from ECMWF (2.27 ± 3.22% $decade^{-1}$) and NCEP (2.52 ± 2.35% $decade^{-1}$). In the temperate region, GPS-derived PWV trend (1.46 ± 0.78% $decade^{-1}$) is very close to that from ECMWF (1.42 ± 0.60% $decade^{-1}$) but greater than that from NCEP (1.19 ± 0.65% $decade^{-1}$). This may be due to the fact that GPS stations have a significantly inhomogeneous distribution. As seen in Figure 2, most of the GPS stations (73 out of 100 sites) are located in the temperate region, especially in the Northern Hemisphere. There are only 17 and 10 GPS stations located at the tropical and polar regions, respectively. The uneven distribution of GPS stations may suggest that the GPS-derived PWV change trends in the tropical and polar regions are probably not as statistically representative as that in the temperate region.

4.3. Relationship Between PWV and Surface Temperature

According to the Clausius-Clapeyron equation, the water-holding capacity of the atmosphere increases by about 7% on global domain for every 1 K rise in temperature [*Trenberth et al.*, 2003]. Many studies have demonstrated that water vapor trends are strongly linked to changes in surface temperature [*Trenberth et al.*, 2005; *Dai*, 2006; *Wagner et al.*, 2006; *Lu et al.*, 2015]. This paper thus further studies the relationship between global PWV change and the surface temperature change.

Table 3. PWV Changes Corresponding to 1 K Temperature Rise Estimated Using ECMWF Surface Temperature and PWV Data From the ECMWF, NCEP, Radiosonde, GPS, and Microwave Satellite, Respectively (Unit: mm K^{-1})[a]

		Trend		
Data Source	Coverage	1979–2014	1992–2014	2000–2014
ECMWF	Global	*0.44 ± 0.31 (2.4 ± 1.7%)* ***0.17 ± 0.05***	*1.21 ± 0.26 (6.6 ± 1.4%)* ***0.28 ± 0.08***	*1.85 ± 0.49 (10.1 ± 2.7%)* ***0.21 ± 0.15***
	Land	*0.37 ± 0.15 (2.4 ± 1.0%)* ***0.20 ± 0.07***	*0.63 ± 0.23 (4.1 ± 1.5%)* ***0.30 ± 0.11***	*0.99 ± 0.50 (6.4 ± 3.2%)* **0.18 ± 0.22**
	Ocean	*0.53 ± 0.49 (2.6 ± 2.4%)* ***0.16 ± 0.04***	*1.74 ± 0.32 (8.7 ± 1.6%)* ***0.27 ± 0.07***	*2.27 ± 0.50 (11.3 ± 2.5%)* ***0.23 ± 0.15***
NCEP	Global	*0.83 ± 0.26 (4.5 ± 1.4%)* ***0.30 ± 0.06***	*1.48 ± 0.29 (7.9 ± 1.5%)* ***0.44 ± 0.10***	*2.16 ± 0.56 (11.4 ± 2.9%)* ***0.24 ± 0.16***
	Land	*0.55 ± 0.18 (3.7 ± 1.2%)* ***0.37 ± 0.09***	*0.92 ± 0.29 (6.1 ± 1.9%)* ***0.51 ± 0.15***	*1.28 ± 0.82 (8.4 ± 5.4%)* **0.24 ± 0.25**
	Ocean	*1.01 ± 0.35 (4.8 ± 1.7%)* ***0.27 ± 0.05***	*1.74 ± 0.35 (8.4 ± 1.7%)* ***0.40 ± 0.08***	*2.15 ± 0.58 (10.3 ± 2.8%)* ***0.24 ± 0.14***
Radiosonde	Land	*0.66 ± 0.32 (3.4 ± 1.6%)*	*1.03 ± 0.49 (5.4 ± 2.6%)*	*1.02 ± 0.97 (5.3 ± 5.0%)*
GPS	Land	--	--	*0.97 ± 0.96 (5.6 ± 5.5%)*
Satellite	Ocean	--	*2.62 ± 0.92 (10.0 ± 3.5%)*	*3.02 ± 0.76 (11.3 ± 2.8%)*

[a]Values in the parentheses are the relative PWV changes (unit: % K^{-1}). The bold values are the surface temperature trends (unit: K $decade^{-1}$) estimated from ECMWF or NCEP. The changes presented in italics indicate that they are statistically significant at the 95% confidence level.

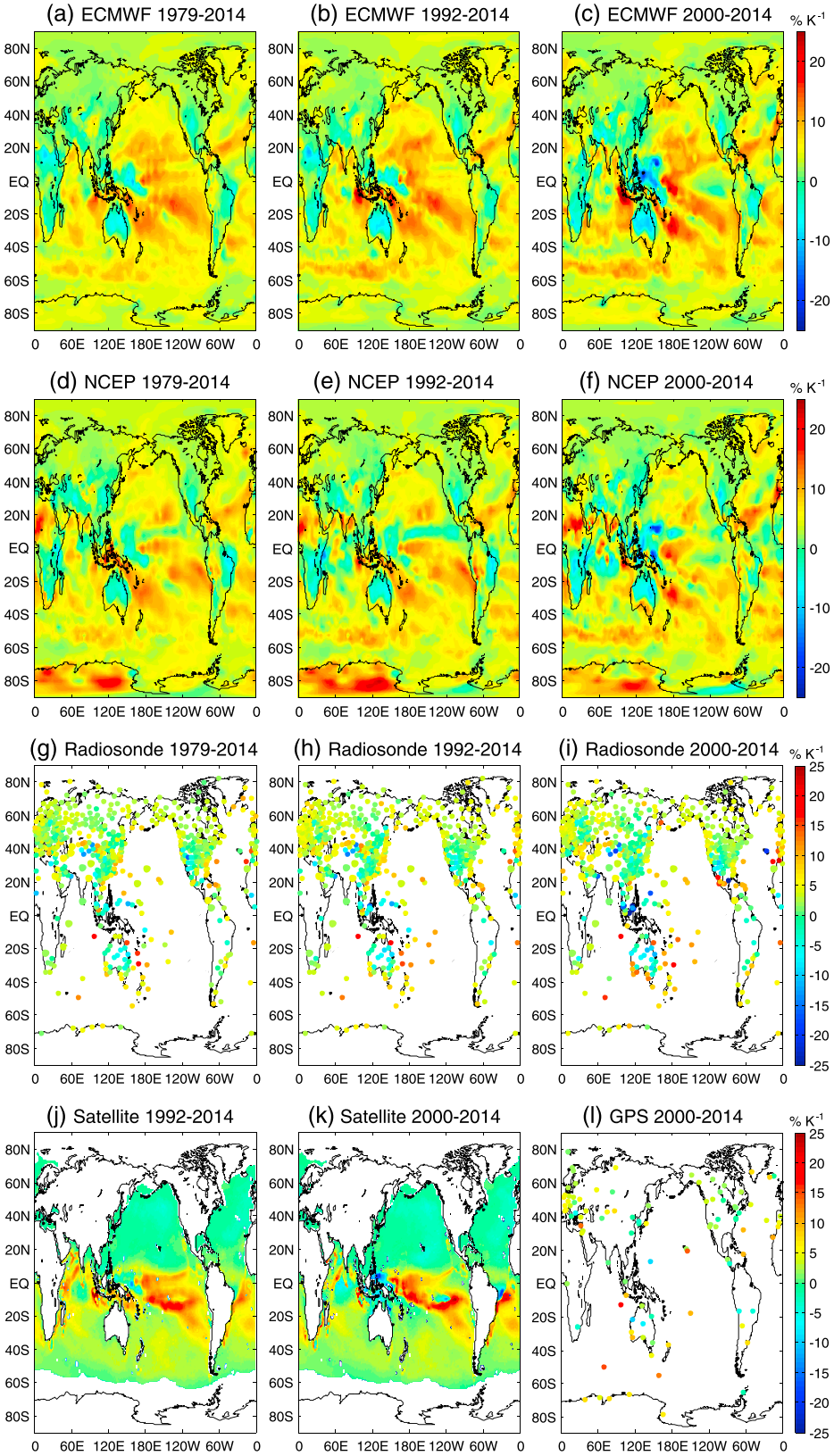

Figure 10. Relative PWV changes with surface temperature rise of 1 K. The 36 year surface temperature data are obtained from the ERA-Interim reanalysis. PWV data are derived from (a–c) ECMWF, (d–f) NCEP, (g–i) radiosonde, (j, k) microwave satellite, and (l) GPS.

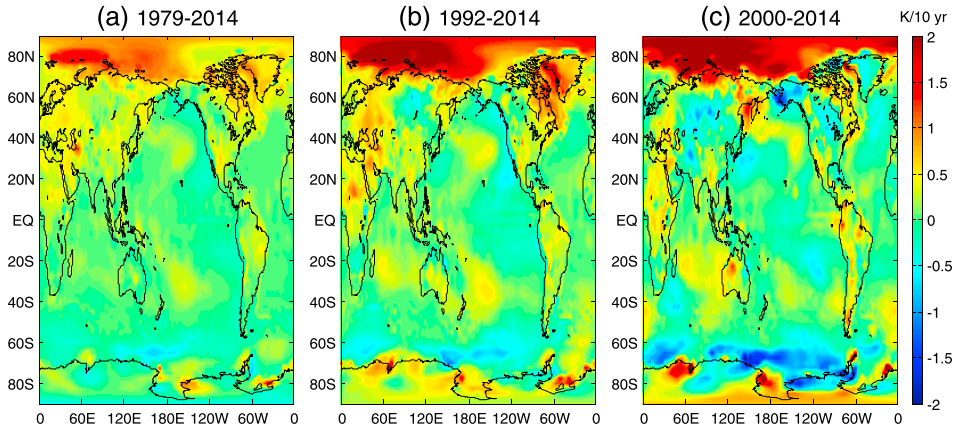

Figure 11. Surface temperature trends (unit: K decade^{-1}) from ERA-Interim for the three periods: (a) 1979–2014, (b) 1992–2014, and (c) 2000–2014.

Based on the 36 year ECMWF ERA-Interim reanalysis data set from 1979 to 2014, the relative changes of global PWV for 1 K rise in temperature are simulated according to the Clausius-Clapeyron equation. For each grid point, surface temperature, temperature lapse rate, and relative humidity profile are derived by averaging the 36 year data. By using these parameters, PWV can be integrated for each grid point. We increase the surface temperature by 1 K and assume the conservation of relative humidity, and the corresponding PWV changes are then derived for every grid points. PWV increases of 8.0%, 8.5%, and 7.8% K^{-1} are obtained for global, land, and oceanic regions, respectively. Figure 9 presents spatial patterns of global PWV changes. The global PWV increases range from 6% to 13% for temperature rise of 1 K. The largest PWV increases occur in the Antarctic (deep red), and the smallest increases occur in the tropical Pacific (deep blue). In polar and high terrain regions (e.g., Tibetan Plateau), PWV is more sensitive to temperature increase since climate is dry and cold in these regions.

With the surface temperature increase, however, we may not necessarily obtain the corresponding PWV increase pattern as the Clausius-Clapeyron relation suggests. Especially over the land, opposite trends between the PWV and surface temperature are often found since this relation is more dominated by local nonthermodynamic effects such as long-range transport of air masses, surface type, and water availability [*Wagner et al*., 2006; *Lu et al*., 2015]. With the use of surface temperature data from the ERA-Interim reanalysis and PWV from the five data sets, the relationship between surface temperature and PWV is analyzed. Table 3 gives the coefficients of linear regression between PWV change and surface temperature change over the global, land, and oceanic regions for the three periods. For the period 1979–2014, the regression slopes derived from ECMWF and NCEP over the globe are $2.4 \pm 1.7\%$ K^{-1} and $4.5 \pm 1.4\%$ K^{-1}, respectively. This regression slope intensifies greatly in the recent years as values of $10.1 \pm 2.7\%$ K^{-1} and $11.4 \pm 2.9\%$ K^{-1} are yielded from the ECMWF and NCEP for 2000–2014, respectively. Over the land, the radiosonde-derived PWV-temperature regression slopes are larger than those from ECMWF and smaller than those from NCEP for the periods 1979–2014 and 1992–2014. For the most recent 15 years 2000–2014, both radiosonde and GPS-derived regression slopes are smaller than those from the reanalysis. Strong regression slopes are observed over the ocean from both reanalysis and microwave satellite data. Over the oceanic region, the ECMWF-derived relations are very close to those from the microwave satellite observations and a regression slope 11.3% K^{-1} is estimated from both data sets over the 2000–2014 period. The PWV-temperature relationship is stronger over the ocean than the land. In addition, the surface temperature trends (bold values) estimated from ECMWF/NCEP are also given in Table 3. Positive trends in surface temperature are obtained from both reanalysis data sets for the three periods. Like the PWV, surface temperature trends estimated from NCEP are larger than those derived from ECMWF. However, the surface temperature trends derived from both reanalyses indicate global surface warming slowdown in the recent period 2000–2014.

Figure 10 presents the spatial patterns of the PWV-temperature regression slopes. Positive regression slopes are found over most oceans and the polar regions from both the ECMWF and NCEP reanalyses (Figures 10a–10f). Negative regression slopes are observed over the western United States and northern

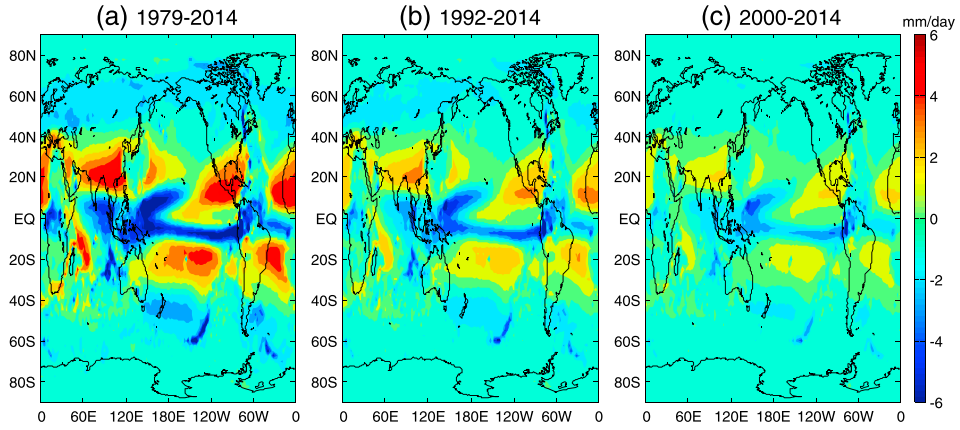

Figure 12. Vertically integrated moisture flux divergences (unit: mm/day) from ERA-Interim for the three periods: (a) 1979–2014, (b) 1992–2014, and (c) 2000–2014.

Mexico, eastern Brazil, most of Mainland China, South China Sea, southern Africa, most of Australia, and western tropical Pacific. In these regions, as shown in Figure 11, surface temperature warming trends occur except for the southern Africa. In regions, i.e., western United States, northern Mexico, eastern Brazil, most of Mainland China, South China Sea, and most of Australia, PWVs show a decrease with surface temperature warming due to high moisture divergence as illustrated in Figure 12. And in southern Africa, PWVs increase with surface temperature cooling because of moisture convergence in this region. For the western tropical Pacific, it is located in the domain of the Intertropical Convergence Zone where extremely high moisture convergences occur (see Figure 12). However, as shown in Figure 11, surface temperature trends in this region are not significant, with values approaching to 0. This large contrast results in the obvious negative PWV-temperature regression slopes in this region. Generally, the highly positive and negative regression slopes exist in regions where high moisture divergences or convergences occur. For the NCEP, very strong positive regression slopes are found over the western Antarctic and northern Africa. The strong positive PWV-temperature regression slope over the northern Africa is not reliable since surface evaporation over the deserts is very weak and could not maintain a constant relative humidity as air temperature increases [*Dai*, 2006]. The regression slopes derived from radiosonde (Figures 10g–10i) and GPS (Figure 10l) at each site are very consistent with those from ECMWF. For example, both radiosonde and GPS show negative regression slopes at the stations located at the Australia and western tropical Pacific. In addition, spatial patterns of the regression slope over the ocean derived from the microwave satellite are displayed in Figures 10j and 10k. Similar with ECMWF, negative patterns are found over the Indian Ocean and western tropical Pacific. Very strong regression slopes are observed over the tropical Pacific. In the recent period 2000–2014, negative regression slopes are seen over some eastern tropical Pacific regions, similar to those observed from the reanalysis.

5. Conclusions

Increasing trends of global water vapor have been observed from the analysis of five types of data sets: 36 year ECMWF ERA-Interim reanalysis data set, 36 year NCEP/DOE AMIP-II reanalysis (R-2), 36 year radiosonde, 23 year microwave satellite, and 15 year GPS data. It has been illustrated that upward PWV trends are becoming more apparent in recent years, which is likely due to various factors including the anthropogenic global warming, large-scale moisture convergence and dynamics, and the relative configuration of tropical convection relative to sea surface temperature. The amount of PWV varies in the range of 0–55 mm depending upon the location, and water vapor experiences larger variations over the land than over the ocean.

PWV data from the ECMWF and NCEP have been evaluated by radiosonde, GPS, and microwave satellite observations. It is shown that ECMWF has better performance than NCEP. In the evaluation by radiosonde, ECMWF and NCEP achieve RMS errors of 2.88 mm and 3.12 mm, respectively. For the comparison with GPS, RMS errors for ECMWF and NCEP are 3.43 mm and 4.13 mm, respectively. Evaluated by microwave satellite

over the oceans, ECMWF and NCEP have RMS errors of 1.65 mm and 3.84 mm, respectively. It is found that ECMWF overestimates the PWV over the ocean before 1992, which is related to changing observing systems and their ability to counter model physics biases. Therefore, ECMWF-derived trends for the period 1979–2014 are not very reliable. The validation also demonstrates that the performances of both reanalysis models are unsatisfactory in the polar region because very limited observations are available in that region for data assimilation.

The PWV trends of the five data sets are analyzed in terms of global, tropical, temperate, and polar regions. For the period 1979–2014, global average PWV trends estimated from the data sets are all positive with the largest upward trend of $0.61 \pm 0.33\%\,\text{decade}^{-1}$ from NCEP and the second largest value of $0.57 \pm 0.28\%\,\text{decade}^{-1}$ from radiosonde. For the period 1992–2014, significantly increased trends of $1.31 \pm 0.47\%\,\text{decade}^{-1}$, $1.58 \pm 0.53\%\,\text{decade}^{-1}$, and $1.67 \pm 1.17\%\,\text{decade}^{-1}$ are observed from ECMWF, NCEP, and radiosonde, respectively. For the recent 15 years, 2000–2014, all the data sets show stronger upward trends in the global PWV with the largest value of $1.84 \pm 0.85\%\,\text{decade}^{-1}$ from the radiosonde. Though there exists a bias in the PWV series between ECMWF and NCEP after 1992, similar PWV trends have been demonstrated by both models.

Polar region has demonstrated the largest PWV increase, suggesting that it has suffered significant impact due to global warming, but the dearth of observational data there precludes a definitive statement. Over the ocean, positive PWV trends of $1.52 \pm 0.61\%$ and $1.62 \pm 0.47\%\,\text{decade}^{-1}$ for the two periods 1992–2014 and 2000–2014 are derived from the microwave satellite observations. They are very close to those derived from ECMWF. Over the past two decades, PWV decrease trends are observed over Asia, the United States, and North Africa. However, large positive PWV trends are found over the north and west Pacific, Europe, the eastern Indian Ocean, and southern Asia.

Based on the 36 year (1979–2014) ERA-Interim reanalysis data set, the simulation of Clausius-Clapeyron relation shows that global PWV should increase in the range of 6%–13% K^{-1} accordingly with air temperature increase. The real-world relationship between surface temperature and PWV is also analyzed using surface temperature data from the ERA-Interim reanalysis and PWV from the five data sets. Global PWV-temperature regression slopes of $2.4 \pm 1.7\%\ K^{-1}$ and $4.5 \pm 1.4\%\ K^{-1}$ are obtained for the period 1979–2014 from ECMWF and NCEP, respectively. The regression slopes grow rapidly in the recent years 2000–2014, and slopes of $10.1 \pm 2.7\%\ K^{-1}$ and $11.4 \pm 2.9\%\ K^{-1}$ are yielded from the ECMWF and NCEP, respectively. Spatial patterns of the PWV-temperature relationship show positive regression slopes over most oceans and the polar region. Negative regression slopes are observed over the western United States, northern Mexico, eastern Brazil, most of Mainland China, South China Sea, southern Africa, most of Australia, and western tropical Pacific. PWV-temperature regression slopes that significantly depart from Clausius-Clapeyron rates are mostly due to the regional moisture divergence/convergence. Generally, steep regression slopes exist in regions where large moisture divergences or convergences occur. At present, the respective contribution of natural and anthropogenic forcings to PWV changes remains unclear. Globally, the PWV increases as global temperature rises, while its change differs greatly on regional scales. Future studies could be carried out on weather regimes and joint probability distribution of PWV and surface temperature to understand processes better.

Acknowledgments

The authors would like to acknowledge the support from the Hong Kong Research Grants Council (RGC) (project PolyU 5325/12E (F-PP0F)), the National Natural Science Foundation of China (project 41274039), and the Hong Kong Polytechnic University (project G-YBM3). The European Centre for Medium-Range Weather Forecasts is appreciated for providing the ECMWF reanalysis data. The National Oceanic and Atmospheric Administration (NOAA) is thanked for providing the IGRA radiosonde data. NCEP_Reanalysis 2 data are provided by the NOAA/OAR/ESRL PSD, Boulder, Colorado, USA, from the website at http://www.esrl.noaa.gov/psd/. The Satellite Application Facility on Climate Monitoring (CMSAF) of European Organization for the Exploitation of Meteorological Satellites (EUMETSAT) is appreciated for providing the HOAPS 3.2 and ATOVS PWV data sets, from the website at https://wui.cmsaf.eu. Finally, the authors want to thank the GFZ German Research Centre for Geosciences for providing the reprocessed GPS ZTD products. The constructive comments from the anonymous reviewers are appreciated for improving the manuscript quality.

References

Adler, R. F., G. Gu, J. Wang, G. J. Huffman, S. Curtis, and D. Bolvin (2008), Relationships between global precipitation and surface temperature on interannual and longer timescales (1979–2006), *J. Geophys. Res.*, *113*, D22104, doi:10.1029/2008JD010536.

Ahrens, C., and P. Samson (2011), *Extreme Weather and Climate*, 1st ed., Brooks Cole, United States of America.

Allan, R. P. (2002), Analysis of moisture variability in the European Centre for Medium-Range Weather Forecasts 15-year reanalysis over the tropical oceans, *J. Geophys. Res.*, *107*(D15), 4230, doi:10.1029/2001JD001132.

Andersson, A., K. Fennig, C. Klepp, S. Bakan, H. Graßl, and J. Schulz (2010), The Hamburg Ocean Atmosphere Parameters and Fluxes from Satellite Data—HOAPS-3, *Earth Syst. Sci. Data*, *2*(2), 215–234, doi:10.5194/essd-2-215-2010.

Bengtsson, L. (2004), Can climate trends be calculated from reanalysis data?, *J. Geophys. Res.*, *109*, D11111, doi:10.1029/2004JD004536.

Beutler, G., M. Rothacher, S. Schaer, T. A. Springer, J. Kouba, and R. E. Neilan (1999), The International GPS Service (IGS): An interdisciplinary service in support of Earth sciences, *Adv. Space Res.*, *23*(4), 631–653, doi:10.1016/S0273-1177(99)00160-X.

Bevis, M., S. Businger, S. Chiswell, T. Herring, R. Anthes, C. Rocken, and R. H. Ware (1994), GPS meteorology: Mapping zenith wet delays onto precipitable water, *J. Appl. Meteorol.*, *33*, 379–386.

Bock, O., F. Guichard, S. Janicot, J. P. Lafore, M.-N. Bouin, and B. Sultan (2007), Multiscale analysis of precipitable water vapor over Africa from GPS data and ECMWF analyses, *Geophys. Res. Lett.*, *34*, L09705, doi:10.1029/2006GL028039.

Chen, B., and Z. Liu (2016), A comprehensive evaluation and analysis of the performance of multiple tropospheric models in China region, *IEEE Trans. Geosci. Remote Sens.*, *54*(2), 663–678, doi:10.1109/TGRS.2015.2456099.

Chung, E.-S., B. Soden, B. J. Sohn, and L. Shi (2014), Upper-tropospheric moistening in response to anthropogenic warming, *Proc. Natl. Acad. Sci. U.S.A.*, *111*(32), 11,636–11,641, doi:10.1073/pnas.1409659111.
Courcoux, N., and M. Schröder (2013), Vertically integrated water vapour, humidity and temperature at pressures levels and layers from ATOVS-daily means/monthly means, Satellite Application Facility on Climate Monitoring, doi:10.5676/EUM_SAF_CM/WVT_ATOVS/V001.
Dai, A. (2006), Recent climatology, variability, and trends in global surface humidity, *J. Clim.*, *19*(15), 3589–3606.
Dee, D. P., et al. (2011), The ERA-Interim reanalysis: Configuration and performance of the data assimilation system, *Q. J. R. Meteorol. Soc.*, *137*, 553–597, doi:10.1002/qj.828.
Deng, Z., G. Gendt, and T. Schöne (2015), Status of the TIGA tide gauge data reprocessing at GFZ, *Int. Assoc. Geod. Symp.*, doi:10.1007/1345_2015_156.
Dessler, A. E., and S. M. Davis (2010), Trends in tropospheric humidity from reanalysis systems, *J. Geophys. Res.*, *115*, D19127, doi:10.1029/2010JD014192.
Doran, P. T., et al. (2002), Antarctic climate cooling and terrestrial ecosystem response, *Nature*, *415*(6871), 514–517.
Duan, J., et al. (1996), GPS meteorology: Direct estimation of the absolute value of precipitable water, *J. Appl. Meteorol.*, *35*(6), 830–838.
Durre, I., R. S. Vose, and D. B. Wuertz (2006), Overview of the integrated global radiosonde archive, *J. Clim.*, *19*(1), 53–68.
Easterling, D., and T. Peterson (1995), A new method for detecting undocumented discontinuities in climatological time series, *Int. J. Climatol.*, *15*, 369–377.
Elgered, G., J. M. Johansson, and B. O. Rönnäng (1997), Measuring regional atmospheric water vapor using the Swedish permanent GPS network, *Geophys. Res. Lett.*, *24*(21), 2663–2666, doi:10.1029/97GL02798.
Fennig, K., A. Andersson, S. Bakan, C.-P. Klepp, and M. Schröder (2012), Hamburg Ocean Atmosphere Parameters and Fluxes from Satellite Data—HOAPS 3.2—Monthly means/6-hourly composites, Satellite Application Facility on Climate Monitoring, doi:10.5676/EUM_SAF_CM/HOAPS/V001.
Fyfe, J. C., et al. (2016), Making sense of the early-2000s warming slowdown, *Nat. Clim. Change*, *6*(3), 224–228.
Guglielmin, M., and N. Cannone (2012), A permafrost warming in a cooling Antarctica?, *Clim. Change*, *111*(2), 177–195, doi:10.1007/s10584-011-0137-2.
Hansen, J., R. Ruedy, M. Sato, M. Imhoff, W. Lawrence, D. Easterling, T. Peterson, and T. Karl (2001), A closer look at United States and global surface temperature, *J. Geophys. Res.*, *106*(D20), 23,947–23,963, doi:10.1029/2001JD000354.
Held, I. M., and B. J. Soden (2006), Robust responses of the hydrological cycle to global warming, *J. Clim.*, *19*(21), 5686–5699.
Intergovernmental Panel on Climate Change (IPCC) (2015), *Climate Change 2014: Synthesis Report, Contribution of Working Groups I, II and III to the Fifth Assessment Report of the Intergovernmental Panel on Climate Change*, edited by Core Writing Team, R. K. Pachauri, and L. A. Meyer, 151 pp., IPCC, Avenue de la Paix 7BIS, Geneva, Switzerland.
Jonas, M., M. Schröder, J. Schulz, A. Andersson, S. Bakan, K. Fennig, and H. K. Grassl Christian-Phillip (2009), Vertically integrated water vapour from SSM/I – Daily/monthly means, Satellite Application Facility on Climate Monitoring, doi:10.5676/EUM_SAF_CM/HTW_SSMI/V001.
Kalany, E., et al. (1996), The NCEP/NCAR 40-year reanalysis project, *Bull. Am. Meteorol. Soc.*, *77*(3), 437–471.
Kanamitsu, M., W. Ebisuzaki, J. Woollen, S.-K. Yang, J. J. Hnilo, M. Fiorino, and G. L. Potter (2002), NCEP–DOE AMIP-II Reanalysis (R-2), *Bull. Am. Meteorol. Soc.*, *83*(11), 1631–1643, doi:10.1175/BAMS-83-11-1631.
Kistler, R., et al. (2001), The NCEP-NCAR 50-year reanalysis: Monthly means CD-ROM and documentation, *Bull. Am. Meteorol. Soc.*, *82*(2), 247–268.
Kuo, Y. H., W. S. Schreiner, J. Wang, D. L. Rossiter, and Y. Zhang (2005), Comparison of GPS radio occultation soundings with radiosondes, *Geophys. Res. Lett.*, *32*, L05817, doi:10.1029/2004GL021443.
Lee, S.-W., J. Kouba, B. Schutz, D. H. Kim, and Y. J. Lee (2013), Monitoring precipitable water vapor in real-time using global navigation satellite systems, *J. Geod.*, *87*(10–12), 923–934, doi:10.1007/s00190-013-0655-y.
Li, J., W. W. Wolf, W. P. Menzel, W. Zhang, H.-L. Huang, and T. H. Achtor (2000), Global soundings of the atmosphere from ATOVS measurements: The algorithm and validation, *J. Appl. Meteorol.*, *39*(8), 1248–1268.
Li, W., Y. Yuan, J. Ou, H. Li, and Z. Li (2012), A new global zenith tropospheric delay model IGGtrop for GNSS applications, *Chin. Sci. Bull.*, *57*(17), 2132–2139, doi:10.1007/s11434-012-5010-9.
Liu, Z., B. Chen, S. T. Chan, Y. Cao, Y. Gao, K. Zhang, and J. Nichol (2015), Analysis and modelling of water vapour and temperature changes in Hong Kong using a 40-year radiosonde record: 1973–2012, *Int. J. Climatol.*, *35*(3), 462–474, doi:10.1002/joc.4001.
Lorenz, C., and H. Kunstmann (2012), The hydrological cycle in three state-of-the-art reanalyses: Intercomparison and performance analysis, *J. Hydrometeorol.*, *13*(5), 1397–1420, doi:10.1175/JHM-D-11-088.1.
Lu, N., J. Qin, Y. Gao, K. Yang, K. E. Trenberth, M. Gehne, and Y. Zhu (2015), Trends and variability in atmospheric precipitable water over the Tibetan Plateau for 2000–2010, *Int. J. Climatol.*, *35*(7), 1394–1404, doi:10.1002/joc.4064.
Mieruch, S., S. Noël, H. Bovensmann, and J. P. Burrows (2008), Analysis of global water vapour trends from satellite measurements in the visible spectral range, *Atmos. Chem. Phys.*, *8*, 491–504.
Mieruch, S., M. Schröder, S. Noël, and J. Schulz (2014), Comparison of decadal global water vapor changes derived from independent satellite time series, *J. Geophys. Res. Atmos.*, *119*, 12,489–12,499, doi:10.1002/2014JD021588.
Mohanakumar, K. (2008), *Stratosphere Troposphere Interactions: An Introduction*, Springer, New York.
Niell, A. E., A. J. Coster, F. S. Solheim, V. B. Mendes, P. C. Toor, R. B. Langley, and C. A. Upham (2001), Comparison of measurements of atmospheric wet delay by radiosonde, water vapor radiometer, GPS, and VLBI, *J. Atmos. Oceanic Technol.*, *18*, 830–850.
Nilsson, T., and G. Elgered (2008), Long-term trends in the atmospheric water vapor content estimated from ground-based GPS data, *J. Geophys. Res.*, *113*, D19101, doi:10.1029/2008JD010110.
Ning, T., R. Haas, G. Elgered, and U. Willén (2011), Multi-technique comparisons of 10 years of wet delay estimates on the west coast of Sweden, *J. Geod.*, *86*(7), 565–575, doi:10.1007/s00190-011-0527-2.
Oikonomou, E. K., and A. O'Neill (2006), Evaluation of ozone and water vapor fields from the ECMWF reanalysis ERA-40 during 1991–1999 in comparison with UARS satellite and MOZAIC aircraft observations, *J. Geophys. Res.*, *111*, D14109, doi:10.1029/2004JD005341.
Parker, D., C. Folland, A. Scaife, J. Knight, A. Colman, P. Baines, and B. Dong (2007), Decadal to multidecadal variability and the climate change background, *J. Geophys. Res.*, *112*, D18115, doi:10.1029/2007JD008411.
Ross, R. J., and W. P. Elliott (1996), Tropospheric water vapor climatology and trends over North America: 1973–93, *J. Clim.*, *9*, 3561–3574.
Ross, R. J., and W. P. Elliott (2001), Radiosonde-based Northern Hemisphere tropospheric water vapor trends, *J. Clim.*, *14*, 1602–1612.
Santer, B. D., et al. (2006), Forced and unforced ocean temperature changes in Atlantic and Pacific tropical cyclogenesis regions, *Proc. Natl. Acad. Sci. U.S.A.*, *103*(38), 13,905–13,910.
Schröder, M., M. Jonas, R. Lindau, J. Schulz, and K. Fennig (2013), The CM SAF SSM/I-based total column water vapour climate data record: Methods and evaluation against re-analyses and satellite, *Atmos. Meas. Tech.*, *6*(3), 765–775, doi:10.5194/amt-6-765-2013.

Screen, J. A., C. Deser, and I. Simmonds (2012), Local and remote controls on observed Arctic warming, *Geophys. Res. Lett.*, *39*, L10709, doi:10.1029/2012GL051598.

Sherwood, S. C., R. Roca, T. M. Weckwerth, and N. G. Andronova (2010), Tropospheric water vapor, convection, and climate, *Rev. Geophys.*, *48*, RG2001, doi:10.1029/2009RG000301.

Smith, T. M., and R. W. Reynolds (2005), A global merged land-air-sea surface temperature reconstruction based on historical observations (1880–1997), *J. Clim.*, *18*(12), 2021–2036.

Soden, B. J., R. T. Wetherald, G. L. Stenchikov, and A. Robock (2002), Global cooling after the eruption of Mount Pinatubo: A test of climate feedback by water vapor, *Science*, *296*, 727–730.

Trenberth, K. E., and L. Smith (2005), The mass of the atmosphere: A constraint on global analyses, *J. Clim.*, *18*(6), 864–875.

Trenberth, K. E., A. Dai, R. M. Rasmussen, and D. B. Parsons (2003), The changing character of precipitation, *Bull. Am. Meteorol. Soc.*, *84*(9), 1205–1217, doi:10.1175/BAMS-84-9-1205.

Trenberth, K. E., J. Fasullo, and L. Smith (2005), Trends and variability in column-integrated atmospheric water vapor, *Clim. Dyn.*, *24*(7–8), 741–758, doi:10.1007/s00382-005-0017-4.

Trenberth, K. E., J. T. Fasullo, and J. Mackaro (2011), Atmospheric moisture transports from ocean to land and global energy flows in reanalyses, *J. Clim.*, *24*(18), 4907–4924, doi:10.1175/2011JCLI4171.1.

Turner, J., J. E. Overland, and J. E. Walsh (2007), An Arctic and Antarctic perspective on recent climate change, *Int. J. Climatol.*, *27*(3), 277–293, doi:10.1002/joc.1406.

Uppala, S. M., et al. (2005), The ERA-40 re-analysis, *Q. J. R. Meteorol. Soc.*, *131*(612), 2961–3012, doi:10.1256/qj.04.176.

Vey, S., R. Dietrich, A. Rülke, M. Fritsche, P. Steigenberger, and M. Rothacher (2010), Validation of precipitable water vapor within the NCEP/DOE Reanalysis using global GPS observations from one decade, *J. Clim.*, *23*(7), 1675–1695, doi:10.1175/2009JCLI2787.1.

Wagner, T., S. Beirle, M. Grzegorski, and U. Platt (2006), Global trends (1996–2003) of total column precipitable water observed by Global Ozone Monitoring Experiment (GOME) on ERS-2 and their relation to near-surface temperature, *J. Geophys. Res.*, *111*, D12102, doi:10.1029/2005JD006523.

Walsh, J. E. (2014), Intensified warming of the Arctic: Causes and impacts on middle latitudes, *Global Planet. Change*, *117*, 52–63, doi:10.1016/j.gloplacha.2014.03.003.

Zhai, P., and R. E. Eskridge (1997), Atmospheric water vapor over China, *J. Clim.*, *10*(10), 2643–2652.

Zhang, L., L. Wu, and B. Gan (2013), Modes and mechanisms of global water vapor variability over the twentieth century, *J. Clim.*, *26*(15), 5578–5593, doi:10.1175/JCLI-D-12-00585.1.

Zhao, T., A. Dai, and J. Wang (2012), Trends in tropospheric humidity from 1970 to 2008 over China from a homogenized radiosonde dataset, *J. Clim.*, *25*(13), 4549–4567, doi:10.1175/JCLI-D-11-00557.1.